

# The effect of hydrogen enrichment on the forced response of CH<sub>4</sub>/H<sub>2</sub>/Air laminar flames

Zhengli Lim<sup>[\*1]</sup>, Jingxuan Li<sup>[\*2]</sup>, Aimee S. Morgans<sup>[\*1]</sup>

<sup>[\*1]</sup>*Department of Mechanical Engineering, Imperial College London*

<sup>[\*2]</sup>*School of Astronautics, Beihang University, Beijing 100083, China*

---

## Abstract

Hydrogen-enrichment of conventional natural gas mixtures is an actively-explored strategy for reducing pollutant emissions from combustion. This study investigates the effect of hydrogen enrichment on the unsteady flame response to perturbations, with a view to understanding the implications for thermoacoustic stability. The Level Set Approach for kinematically tracking the flame front was applied to a laminar conical premixed methane / hydrogen / air flame subjected to 2D incompressible velocity perturbations. For hydrogen enrichment levels ranging from 0% to 80% by volume, the resulting unsteady heat release rate of the flame was used to generate the Flame Describing Functions (FDFs). This was performed across a range of perturbation frequencies and levels at ambient pressure. The mean heat release rate of the flame was fixed at  $\bar{Q} = 2.69$  kW and the equivalence ratio was set to  $\varphi = 1.08$  for all hydrogen enrichment levels. Hydrogen-enrichment was found to shift the FDF gain drop-off to higher frequencies, which will increase propensity to thermoacoustic instability. It also reduced the effective flame time delay. Sensitivity analyses at  $\varphi = 0.8$  revealed that the changes in FDF were driven predominantly by the flame burning speed, and were insensitive to changes in Markstein length.

*Keywords:* Combustion Instabilities, Flame Describing Function, Level Set Approach, Hydrogen

---

\*Author for correspondence: Zhengli Lim – zhengli.lim15@imperial.ac.uk

## 1. Introduction

The combustion of hydrogen-enriched fuel forms an area of increasingly active research interest as gas turbine technology progresses toward fuel decarbonisation [1–4]. The enrichment of conventional hydrocarbon fuels with hydrogen causes significant changes to their base properties, such as diffusivity, heating value and laminar flame burning speed [5, 6], which lead to alterations in the more complex behaviour associated with the combustion of the fuel [5, 7–9]. These include the susceptibility to thermoacoustic instabilities and the conditions under which they occur. Thermoacoustic instabilities, also known as combustion instabilities, have been found to be specifically sensitive to the presence of hydrogen, which burns faster and hotter than conventional natural gas fuel [9–11].

Thermoacoustic instabilities comprise a major challenge faced by modern gas turbines as they produce unwanted effects ranging from reduced performance to component damage [12–14]. The instabilities are an especially apparent side effect for lean premixed combustion [12], which is becoming the preferred route over non-premixed combustion due to tighter regulation of  $\text{NO}_x$  emissions, which are more easily controlled via the former route [15–17]. Thermoacoustic instabilities arise due to the coupling between an unsteady heat source and acoustic waves propagating within a geometry. They occur when the rate of acoustic energy added to the system from the heat source exceeds the rate of acoustic energy lost via transfer across the system boundaries [18, 19].

Multi-scale modelling of thermoacoustic instability is often performed for both efficient computational prediction and to offer insights into instability and how to mitigate it. It comprises two main parts: modelling the flame’s response to velocity perturbations [20, 21], and modelling the acoustic wave propagation within the specified combustor geometry [22]. In the context of understanding thermoacoustic stability changes due to hydrogen enrichment, the multi-scale modelling part more susceptible to changes associated with hydrogen enrichment will be the flame’s response. Furthermore, understanding the dynamics of laminar premixed flames is an important precursor to understanding the dynamics of the turbulent premixed flames that are typically of practical interest [23].

The present work performs a systematic study of the response of a laminar  $\text{CH}_4/\text{H}_2/\text{Air}$  flame to velocity perturbations, under different levels of hydrogen enrichment. It achieves this by combining a kinematic flame model

with an incompressible flow field model. This facilitates computations which are extremely fast compared to turbulent flame studies which employ Large Eddy Simulation (LES) [24–33]. It further facilitates fundamental insights into the parameters governing changes to the flame response, such as laminar flame speed, Markstein length (which directly influences flame burning speed) and bulk velocity, the latter varying in order to maintain constant flame thermal power under varying fuel density and heating value.

## 2. Background Theory

The definition used for equivalence ratio,  $\varphi$ , is,

$$\varphi \equiv \frac{\text{FAR}}{\text{FAR}_{\text{st}}} = \frac{X_{\text{fuel}}/X_{\text{air}}}{(X_{\text{fuel}}/X_{\text{air}})_{\text{st}}} \quad (1)$$

where  $\text{FAR} = X_{\text{fuel}}/X_{\text{air}}$  is fuel-to-air ratio ( $X$  represents mole fraction), and the subscript ‘st’ denotes stoichiometric conditions. Note that the ‘fuel’ here is regarded as the combined  $\text{CH}_4/\text{H}_2$  mixture, such that  $X_{\text{fuel}} = X_{\text{CH}_4} + X_{\text{H}_2}$ . The hydrogen enrichment level,  $\eta_{\text{H}}$ , is defined as,

$$\eta_{\text{H}} \equiv \frac{X_{\text{H}_2}}{X_{\text{CH}_4} + X_{\text{H}_2}} \quad (2)$$

The flame response may be characterised by a ‘Flame Describing Function’ (FDF), also known as a nonlinear Flame Transfer Function (FTF). This takes the normalised velocity perturbation upstream of the flame, characterised by both its frequency and its amplitude, as the input, and the resulting heat release rate fluctuation as the output. The FDF approach assumes that the dominant frequency of the flame response matches that of the upstream velocity forcing, and that the steady-state response is equivalent to the input forcing modified by a gain and phase lag. This may be expressed mathematically as [21, 34],

$$\mathcal{F}(\omega, \beta) \equiv \frac{\hat{Q}'(\omega, \beta)/\bar{Q}}{\hat{u}'_1(\omega)/\bar{u}_1} \quad , \quad \beta \equiv |\hat{u}'_1/\bar{u}_1| \quad (3)$$

where  $\hat{u}'_1(s)$  and  $\hat{Q}'(s, \beta)$  are the upstream velocity perturbation and heat release rate fluctuation at the forcing frequency  $\omega$  respectively, both of which have been transformed into the frequency domain from their time domain

variables  $u_1'(t)$  and  $\dot{Q}'(t)$ . The overbar notation denotes time-averaged quantities.  $\mathcal{F}(s, \beta)$  itself is generally complex-valued and contains information regarding the gain and phase lag imparted by the process.

In the case of laminar flames, turbulence modelling is not required. Several approaches have been devised to solve for the flame kinematics, with one commonly used kinematic model being the ‘G-Equation’ [35–38]. This assumes that the flame is an extremely thin interface, such that a scalar variable,  $G$ , can be used to track the flame surface location. The isocontour  $G = 0$  defines the flame front, which separates fresh reacting flow (denoted by  $G < 0$ ) from the burned gases ( $G > 0$ ):

$$\frac{\partial G}{\partial t} + \vec{u} \cdot \nabla G = s_L |\nabla G| \quad (4)$$

where  $s_L$  is the flame burning speed. The resulting flame surface may be integrated to obtain the heat release rate  $\dot{Q}$ , which is assumed to scale proportionately with surface area  $A$ , such that  $\dot{Q}(t)/\bar{Q} = A(t)/\bar{A}$ . Recently, when combined with an appropriate model for the incompressible velocity field, this was shown to predict the FDF of a laminar conical methane/air flame [39], in strong agreement with experimental results [40].

The flame burning speed  $s_L$  may be treated as the base laminar flame speed, modified by the Markstein parameter which accounts for local flame curvature [41, 42],

$$s_L = s_{L0}(1 - \mathcal{L}\kappa) \quad (5)$$

where  $s_{L0}(T, P, \varphi, \eta_H)$  is the plane laminar flame speed,  $\kappa = \nabla \cdot \nabla G / |\nabla G|$  is the local flame curvature and  $\mathcal{L}(T, P, \varphi, \eta_H)$  is the ‘Markstein length’, which is a length scale describing the thermal thickness of the flame. Both  $s_{L0}$  and  $\mathcal{L}$  are functions of both the thermal conditions and fuel composition.

### 3. Methodology

#### 3.1. Principal Test Case

We consider a conical flame with its base rooted to a cylindrical burner of diameter  $D$ . Premixed  $\text{CH}_4/\text{H}_2/\text{Air}$  is fed into the burner of composition defined by  $(\varphi, \eta_H)$  at an upstream velocity of  $u_1(t) = \bar{u}_1 + u_1'(t)$ , where  $\bar{u}_1$  and  $u_1'(t)$  are the mean and fluctuating components respectively. This is illustrated in Figure 1.

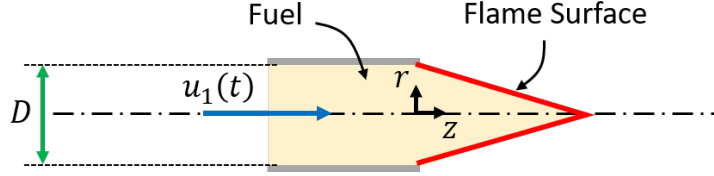


Figure 1: Illustration of test case.

The kinematic response of the flamefront to the upstream velocity fluctuations is simulated using the G-Equation (equation (4)), solved using the Level Set Approach (LSA) [41].

Downstream of the burner exit, a two-dimensional flow field is considered, such that  $\vec{u}(z, r, t) = [u_z, u_r]$ , where  $u_z$  is the major axial component and  $u_r$  is the minor radial component. It has been established that an incompressible flow field assumption is reasonable for modelling the flame response [20, 37]. In addition to this, the coupling between the flame kinematics and the flow field itself may be neglected, such that independent forcing functions for  $\vec{u}$  may be applied [39, 43],

$$u_z(z, t) = \bar{u}_1 + u'_1 = \bar{u}_1 + \hat{u}_1 \cos(kz - \omega t) \quad (6)$$

$$u_r(z, r, t) = u'_r = k \frac{r}{2} \hat{u}_1 \sin(kz - \omega t) \quad (7)$$

where  $\hat{u}_1$  is the perturbation amplitude, which is varied as a parameter once normalised into  $\beta = \hat{u}_1/\bar{u}_1$ .  $\omega$  is the perturbation angular frequency and  $k = \omega/\bar{u}_1$  is the wavenumber. The model has been validated by Direct Numerical Simulation [44].

### 3.2. Selection of Variables and Constraints

The burner diameter was set at  $D = 22$  mm for all simulations. As the main focus of this work is the effect of  $\eta_H$  on  $\mathcal{F}$ , the equivalence ratio was fixed  $\varphi = 1.08$ , and the hydrogen enrichment level was tested across five hydrogen enrichment levels,  $\eta_H = [0 : 0.2 : 0.8]$ , for a total of 5 FDFs. The mean upstream velocity  $\bar{u}_1$  was varied based on fuel composition to satisfy the constraint of a constant mean heat release rate of  $\bar{Q} = 2.69$  kW. Inlet thermal conditions were fixed at a temperature and pressure of  $T_{\text{in}} = 300$  K and  $P_{\text{in}} = 1$  atm. We note that the chosen test burner geometry, equivalence ratio and flame power, along with the incompressible velocity model

of Equations (6) and (7), correspond to those for which the G-equation recently yielded excellent agreement with the experimentally measured FDF for a methane/air flame [39]. This provides confidence in the main assumptions underpinning the approach.

For identification of the FDF, harmonically forced simulations were performed by implementing Equations (6) and (7) over 16 forcing frequencies,  $f_p = \omega/2\pi = [10 : 10 : 160]$  Hz and four amplitude perturbation levels,  $\beta = [0.036, 0.071, 0.143, 0.214]$ . This implies a total of  $4 \times 16 = 64$  data points per FDF.

At this point, we make some comments on hydrogen’s exceptionally low density. While the effect of hydrogen’s density is fully accounted for in terms of the reactant density, velocity and flow rate and hence on the burner power, the G-equation neglects density effects on the kinematic response of the flame. This means that in terms of the flame’s forced response, the density is assumed constant throughout space and equal to that of the reactant mixture. This assumption has been shown sufficiently accurate for methane/air flames ( $\eta_H = 0$ ) [39, 40]. For the hydrogen-enriched compositions tested in this study, the reactant mixture density remains within 10% of the  $\eta_H = 0$  case up to  $\eta_H = 0.6$ , with the  $\eta_H = 0.8$  case showing a 16% deviation. This was assumed sufficiently small for the assumption to remain reasonable. We note that the G-equation is not able to account for Darrius-Landau or thermodiffusive instabilities [45, 46] which, although often of relevance to hydrogen-rich flames, are beyond the scope of the current work.

The Markstein length was fixed at  $\mathcal{L} = 1$  mm for the main study. Although  $\mathcal{L}$  is known to vary according to the mixture state, it is shown in Section 4.2 that its variations do not significantly affect the overall results.

Table 1 summarises the simulation parameters examined in the main study. Note that  $\bar{u}_1$  and  $s_{L0}$  are not independent variables here but are computed based on  $(\varphi, \eta_H)$  and the heat release rate constraint set for this study.

Table 1: Summary of simulation parameters for the main study.

$\varphi$	$\eta_H$	$\beta$	$f_p$ [Hz]	$\bar{u}_1$ [m s <sup>-1</sup> ]	$s_{L0}$ <sup>[*2]</sup> [m s <sup>-1</sup> ]	$\mathcal{L}$ [mm]
1.08	0.0	[*1]	10:10:160	2.12	0.3859	1.00
1.08	0.2	0.036	10:10:160	2.13	0.4494	1.00
1.08	0.4	0.071	10:10:160	2.15	0.5538	1.00
1.08	0.6	0.143	10:10:160	2.18	0.7523	1.00
1.08	0.8	0.214	10:10:160	2.22	1.2175	1.00

[\*1] Note that all four  $\beta$  values listed were tested for each  $\eta_H$  value.

[\*2] Evaluated by Cantera, see Section 3.3 for details.

### 3.3. Numerical Solution Method

The plane laminar flame speed  $s_{L0}$  was evaluated for each unique fuel state using the open-source chemical kinetics code ‘Cantera’ [47], coupled with the GRI-Mech 3.0 mechanism, utilised predominantly for natural gas combustion [48]. Figure 2 shows the computed  $s_{L0}$  values produced by Cantera for the domain  $\eta_H = [0, 1]$ , both at the main test case equivalence ratio of  $\varphi = 1.08$ , and at the equivalence ratio considered in Section 4.2 of  $\varphi = 0.8$ . The results are corroborated by those of Dong et al. [49], whose experimental data best-fit curves are shown alongside the predictions by Cantera. Noting that a significant margin of error was expected in the experimental data, this study used the predictions by Cantera, which were deemed sufficiently accurate for the test cases under consideration.

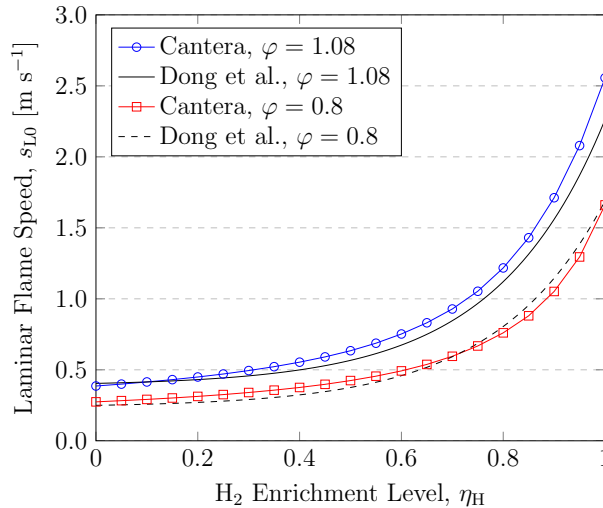


Figure 2: Comparison of laminar flame speeds determined by Cantera and experimentally.

The G-Equation model (Equation 4) was solved with a global spatial step of  $\Delta x = 0.5$  mm and temporal step of  $\Delta t = \Delta x/40 = 1.25 \times 10^{-5}$  s to ensure stability for the range of convective velocities considered.  $G$  was solved spatially using a “fifth-order Weighted Essentially Non-Oscillatory (WENO)” scheme [50] and temporally using a “third-order Total Variation Diminishing (TVD) Runge-Kutta” scheme [51].

The unforced flames were first generated by setting  $\beta = 0$  across  $\eta_H = [0 : 0.2 : 0.8]$ . These plots are shown in Figure 3, and show that the axial flame length decreases as  $\eta_H$  is increased, supporting numerous experimental observations [52].

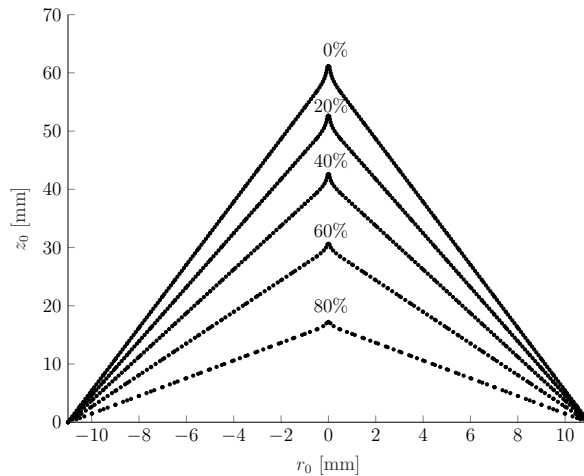


Figure 3: Unforced flame fronts at  $\varphi = 1.08$  as  $\eta_H$  is varied from 0 – 80%. The flame becomes shorter as  $\eta_H$  increases.

Subsequently, forcing was introduced. Each simulation was time-marched until the flame response was observed to settle from its initial transients into periodic oscillatory behaviour. Figure 4 shows an example of the flame response function produced from an arbitrarily chosen simulation. Note that the normalised heat release rate as shown in Figure 4 is computed as the ratio of the instantaneous heat release rate  $\dot{Q}(t)$  to that of the unforced case  $\dot{Q}_0$ , the latter of which is assumed approximately equal to the mean heat release rate, such that  $\bar{Q} \approx \dot{Q}_0$ . Figure 5 shows examples of the flame front evolution corresponding to the periodic heat release rate in Figure 4.



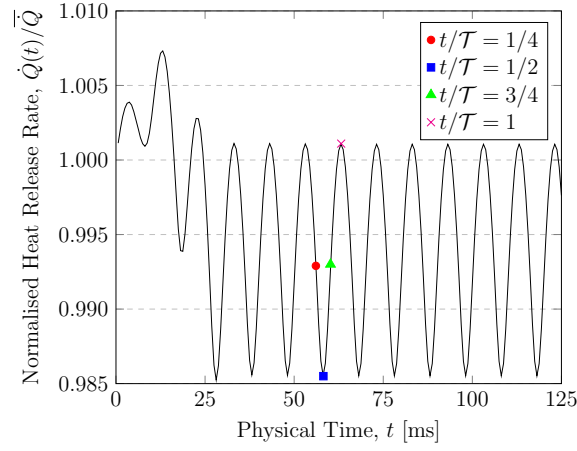


Figure 4: Example of a flame response function for  $(\varphi, \eta_H, \beta, f_p) = (1.08, 0, 0.036, 100)$  with data points corresponding to flame front instances as shown in Figure 5.

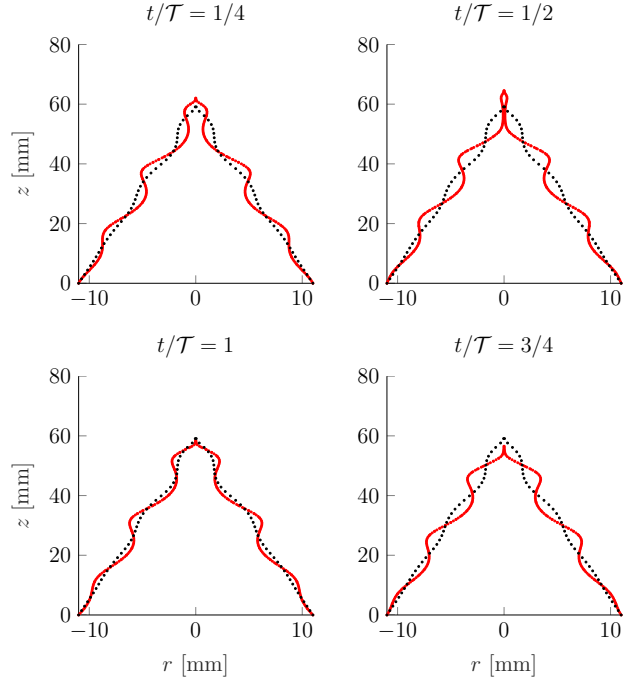


Figure 5: Example of flame front evolution per forcing cycle for  $(\varphi, \eta_H, \beta, f_p) = (1.08, 0, 0.036, 100)$ , corresponding to heat release rate points as shown in Figure 4. Plots in solid red and black dotted lines correspond to the instantaneous and time-mean flame fronts respectively.

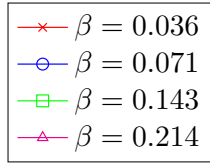
The FDF gain  $|\mathcal{F}|$  was determined as the ratio of the steady-state amplitude of  $\dot{Q}(t)/\bar{Q}$  to the perturbation level  $\beta$ . The phase shift  $\angle\mathcal{F}$  relative to the major axial perturbation was determined by cross-correlation of the two functions.

## 4. Results and Discussion

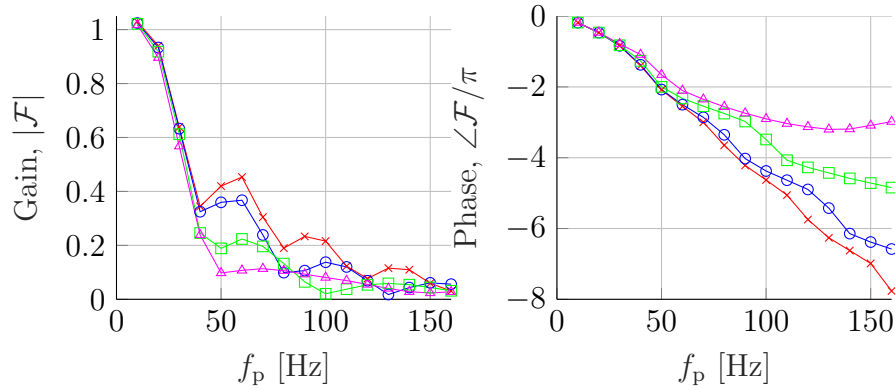
### 4.1. FDF Results

The FDF gain and phase are shown in Figure 6, with each row of plots corresponding to a given value of  $\eta_H$ , with  $\eta_H$  increasing in increments of 0.2;  $\eta_H = [0 : 0.2 : 0.8]$ . Each of the curves on the FDF plot corresponds to one of the four  $\beta$  values tested. The FDF for  $\eta_H = 0$  corroborates that found by Li & Morgans [39].

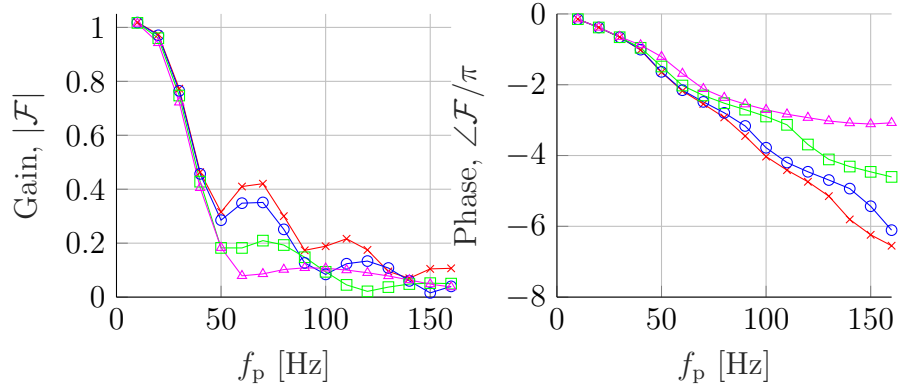
Three main observations regarding the effect of hydrogen enrichment on the flame response can be drawn from the results. An increase in hydrogen enrichment causes: (i) an increase in cut-off frequency, (ii) a decrease in phase lag and, (iii) a reduction in non-linearity.



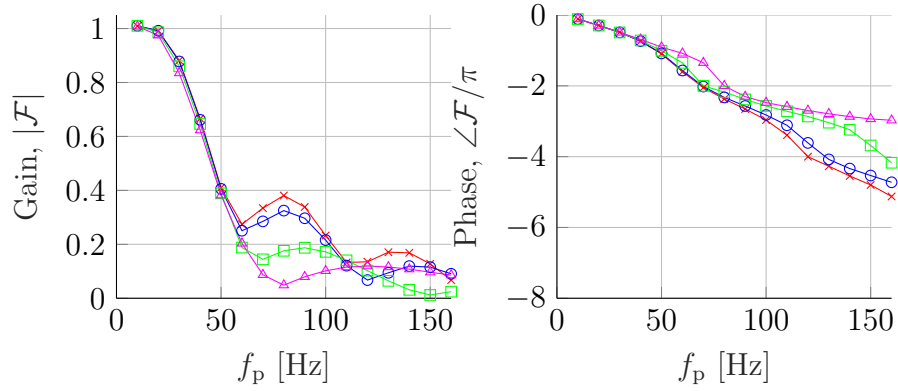
(a),(b) – 0% Hydrogen Enrichment



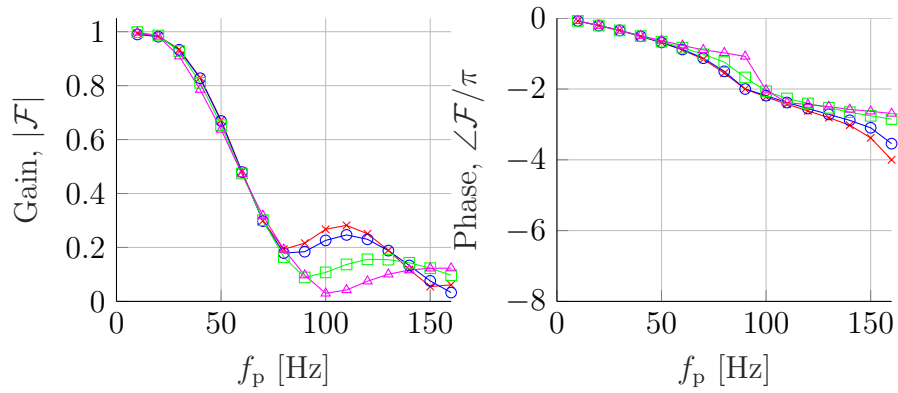
(c),(d) – 20% Hydrogen Enrichment



(e),(f) – 40% Hydrogen Enrichment



(g),(h) – 60% Hydrogen Enrichment



(i),(j) – 80% Hydrogen Enrichment

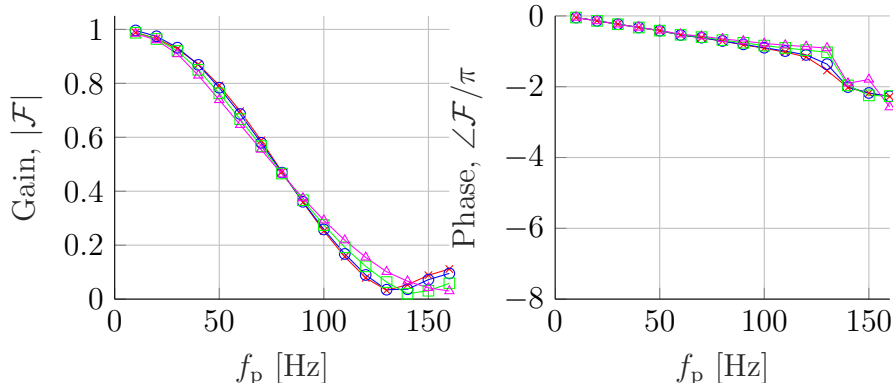


Figure 6: Flame Describing Functions for varying hydrogen enrichment,  $\eta_{\text{H}}$ . Each row of plots corresponds to a different value of  $\eta_{\text{H}}$ , with the top row corresponding to  $\eta_{\text{H}} = 0$  and  $\eta_{\text{H}}$  increasing for subsequent rows by 0.2, up to a final value of 0.8.

From the gain plots, hydrogen enrichment is seen to increase the threshold frequency at which gain drop-off occurs. The consequence of this is that systems involving hydrogen-enriched fuel are likely to exhibit increased propensity to thermoacoustic instability – a finding that is corroborated by other numerical studies on hydrogen-enriched fuels [53–56].

From the phase plots, hydrogen enrichment is seen to decrease the phase lag between the perturbation and the response. This is consistent with the fact that increased hydrogen content produces shorter flames (Figure 3), leading to lower convection times associated with the response, in corroboration with the findings of [57]. The thermoacoustic stability of a combustor depends on strongly the phase of the FDF, but in a more complicated manner, with the Rayleigh criterion source term depending on the phase between the heat release rate and acoustic pressure perturbation at the flame [18]. The latter depends on the acoustic modeshape of the relevant mode within the combustor, and so cannot be predicted from the flame response alone. Thus while it can be said that the reduced phase will affect the thermoacoustic stability, the direction of this effect will depend on the geometry of the combustor within which the flame is placed.

Finally, both plots show that hydrogen enrichment suppresses the dependence of  $\mathcal{F}$  on the perturbation level  $\beta$ , as the four curves on each plot converge toward a single curve as hydrogen content increases. However, it was noted that all plots show that the curves begin converging at low perturbation frequencies, and diverge upon crossing a threshold frequency, this

threshold increasing with hydrogen enrichment. Hence, it is very likely that non-linearity is not wholly suppressed but instead shifted to higher frequencies.

The increase in the gain drop-off frequency for hydrogen-enriched flames was determined a trait of interest to analyse further. Hence, flame front evolution tracking was performed for the two test cases  $\eta_{\text{H}} = 0$  and  $\eta_{\text{H}} = 0.6$ , both held at  $(\varphi, \beta, f_{\text{p}}) = (1.08, 0.071, 40)$ . The 40 Hz frequency was chosen because the gain of the  $\eta_{\text{H}} = 0$  case was relatively low at that frequency, being beyond the drop-off frequency, while the gain of the  $\eta_{\text{H}} = 0.6$  case remained relatively high. The resulting flame front snapshots are shown in Figure 7, with the  $\eta_{\text{H}} = 0$  case plotted in solid red and the  $\eta_{\text{H}} = 0.6$  case plotted in solid blue. Note that the snapshots  $t/\mathcal{T} = 1/2$  and  $t/\mathcal{T} = 1$  correspond to the minimum and maximum normalised heat release rate states respectively.

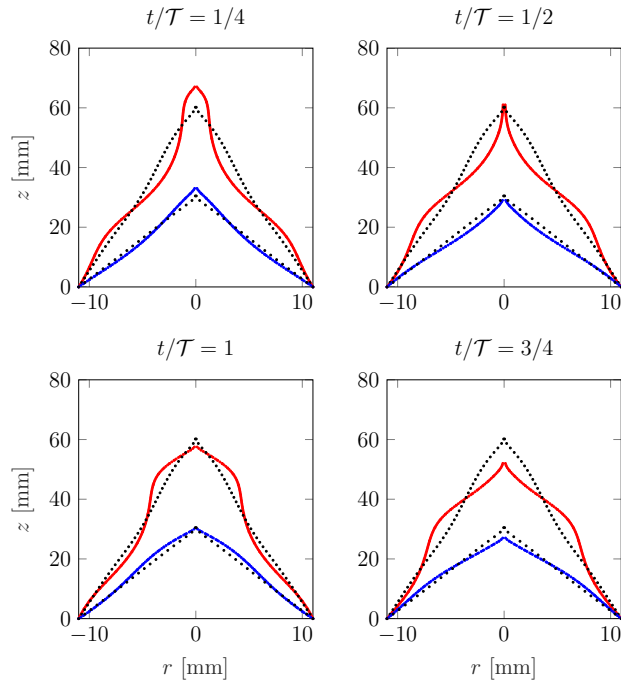


Figure 7: Comparison of  $\eta_{\text{H}} = 0$  (red) and  $\eta_{\text{H}} = 0.6$  (blue) flame front evolution for one forcing cycle at  $(\varphi, \beta, f_{\text{p}}) = (1.08, 0.071, 40)$ . Axial flame length decreases with increasing  $\eta_{\text{H}}$ . Plots in solid and dotted lines correspond to the instantaneous and time-mean flame fronts respectively.

First, the similarities between the two cases were noted. Namely, the

flame surface area (and consequently the heat release rate) depends on two features of the flame front: 1. the overall tip length, and 2. the concavity of the region leading up to the flame tip. A greater flame tip length allows more area to be covered over the axial span. Additionally, a flame shape that maintains a relatively large radius along its axial length has a larger surface area since  $\delta A \propto 2\pi r \delta z$ . The result is that the final flame surface area is governed by the combination of these two factors.

The  $t/\mathcal{T} = 1/4$  and  $t/\mathcal{T} = 3/4$  snapshots represent times when the gain is at its mean value, and it was noted that the two mechanisms mentioned are competing at these times. At,  $t/\mathcal{T} = 1/4$ , the flame tip length is at its highest, but this is undermined by the concavity of the flame which decays to lower radii relatively quickly. The opposite is true at  $t/\mathcal{T} = 3/4$ . In contrast, the maximum and minimum gains occur when both mechanisms act constructively.

As for the differences, it was noted that the  $\eta_{\text{H}} = 0$  flame exhibited a greater distortion of curvature from the mean shape at all times, while the  $\eta_{\text{H}} = 0.6$  flame retained a profile more closely resembling its unforced shape. It is shown in Section 4.3 that the higher laminar flame speed of hydrogen-enriched fuel is by far the dominant driver behind such differences. Hence, it can be postulated that the higher flame burning speed of the  $\eta_{\text{H}} = 0.6$  case acts to stabilise the flame against distortion by a given perturbation.

It may appear counter-intuitive that the  $\eta_{\text{H}} = 0.6$  case is the one with higher gain when comparing the cases on an absolute scale. A fairer comparison was achieved by creating dimensionless plots of the flame fronts, with  $z/z_0$  against  $r/D$ , where  $z_0$  is the axial distance from the base to the unforced flame tip. This is shown in Figure 8.

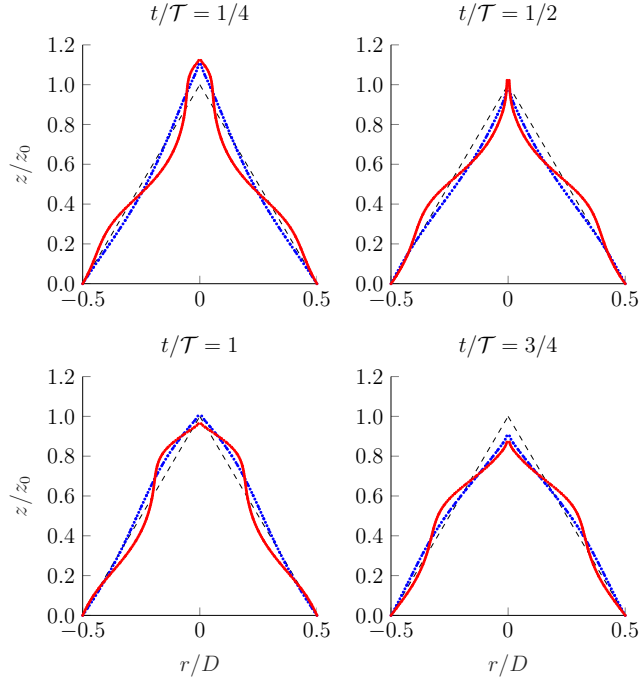


Figure 8: Dimensionless plots of  $\eta_H = 0$  (red) and  $\eta_H = 0.6$  (blue) flame fronts for one forcing cycle at  $(\varphi, \beta, f_p) = (1.08, 0.071, 40)$ . Plots in solid and dotted lines correspond to the instantaneous and time-mean flame fronts respectively.

Within the dimensionless plots, the flame tip lengths were observed to approximately match across both cases at all times. While greater curvature does lead to a greater surface area in absolute terms, it is important to note that the gain is effectively determined by the difference between the maximum and minimum areas obtained in a cycle. Although the  $\eta_H = 0$  flame displays significantly more curvature distortion than the  $\eta_H = 0.6$  case, this distortion increases both its maximum and minimum areas in absolute terms, but may not necessarily translate to a greater difference between the two. It was observed in this case that the curvature-distortion of the flame actually dampened the driving mechanisms of area fluctuation, resulting in a lower gain.

Figure 9 shows the dimensionless plots of  $\Delta A/A_0$  against  $z/z_0$  for both flames at various points in the forcing cycle, where  $A_0$  is the unforced flame surface area. The dimensionless quantity  $\Delta A/A_0$  denotes the relative contribution of a flame section (at a given axial location) to the total flame

surface area. Since the total area  $A$  of the flame is calculated by numerically integrating across the grid points of spatial step  $\Delta x$ , the area contribution between any two such points is calculated as  $\Delta A$ . This means that a higher value of  $\Delta A/A_0$  at a given  $z/z_0$  signifies a greater contribution to the normalised flame surface area at that location. Note that  $A_0 = 210 \text{ mm}^2$  and  $110 \text{ mm}^2$  for the  $\eta_H = 0$  and  $0.6$  flames respectively. The plots in Figure 9 are consistent with the suggestion that the greatest contribution to the flame surface area occurs at the base.

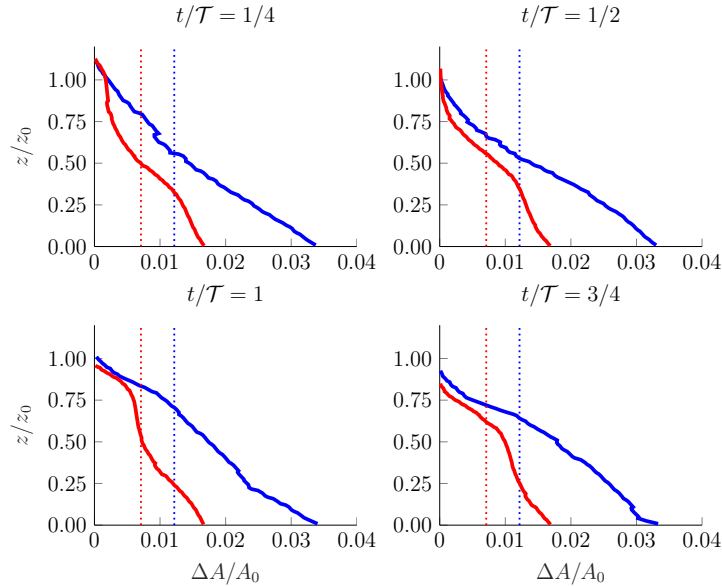


Figure 9: Dimensionless plots of surface area contribution as a function of the axial coordinate,  $z$ , for  $\eta_H = 0$  (red) and  $\eta_H = 0.6$  (blue) during a forcing cycle. Dotted lines represent the mean values.

The absolute and dimensionless area fluctuations,  $A'(t)$  and  $A'(t)/A_0$ , are shown over one forcing period in Figure 10. It can be seen that both the absolute and dimensionless fluctuations for the  $\eta_H = 0.6$  case exceed those of the  $\eta_H = 0$  case, supporting the idea that the higher local curvature of the latter (as observed in Figures 7 and 8) does not necessarily imply greater deviations in the total flame surface area.



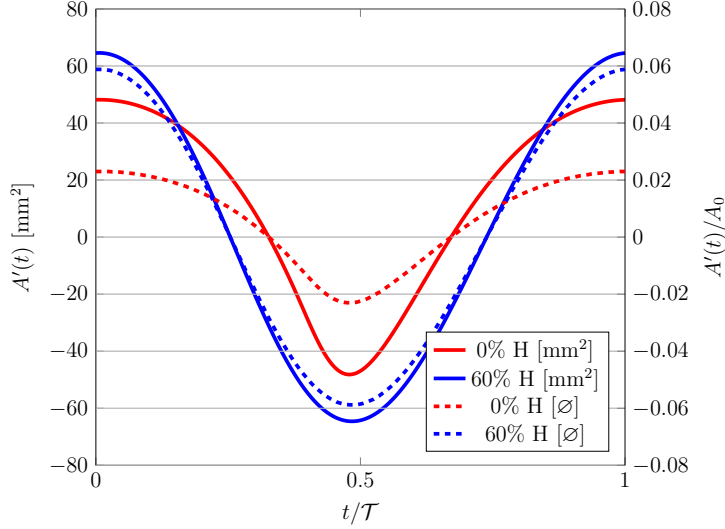


Figure 10: Absolute and dimensionless flame surface area fluctuations across one period at  $f_p = 40$  Hz.

#### 4.2. Sensitivity of Results to Markstein Length

The FDF results obtained in Figure 6 were based on the assumption of a constant Markstein length of  $\mathcal{L}_{ct} = 1$  mm. This assumption is now investigated by conducting a separate analysis at an equivalence ratio of 0.8, this corresponding to one where the actual Markstein lengths  $\mathcal{L}_{act}$  are known [58]. A low forcing amplitude level of  $\beta = 0.071$  is used, enabling the flame transfer function (FTF) rather than the more complicated FDF to be compared. The FTFs were calculated across the same frequency range,  $f_p = 10 : 10 : 160$  Hz, using both the actual and assumed Markstein lengths, with the hydrogen content varying from  $\eta_H = [0 : 0.2 : 0.6]$ , as summarised in Table 2.

Table 2: Summary of simulation parameters for the Markstein length sensitivity analysis.

$\varphi$	$\eta_H$	$\beta$	$f_p$ [Hz]	$\mathcal{L}_{act}$ [mm]	$\mathcal{L}_{ct}$ [mm]
0.8	0.0	0.071	10:10:160	0.56	1.00
0.8	0.2	0.071	10:10:160	0.34	1.00
0.8	0.4	0.071	10:10:160	0.12	1.00
0.8	0.6	0.071	10:10:160	-0.11	1.00

The resulting FTFs are shown in Figure 11. Note that solid line plots

represent the FTFs produced with  $\mathcal{L}_{\text{act}}$ , while dashed line plots represent the FTFs produced with  $\mathcal{L}_{\text{ct}}$ . The forcing frequency is expressed in its dimensionless form, the flame Strouhal number,  $St \equiv f_p D / s_{L0}$ .

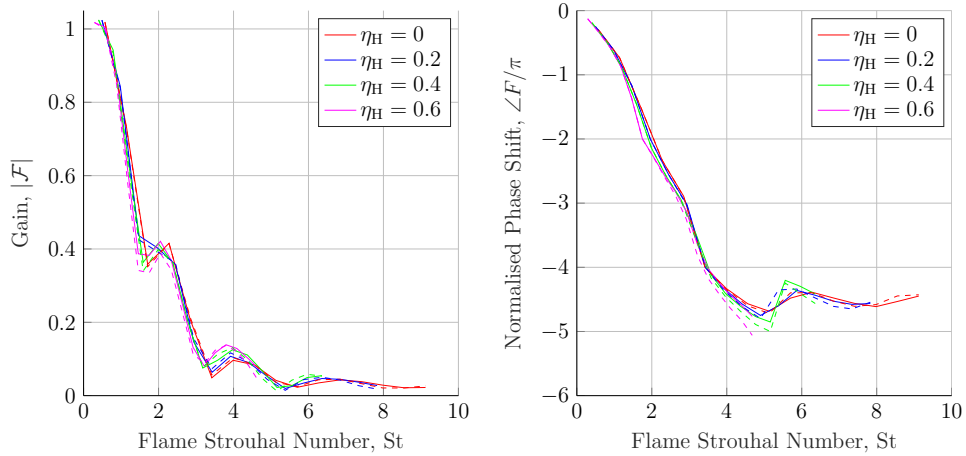


Figure 11: Comparison of Flame Transfer Functions with actual (solid lines) against assumed (dashed lines) Markstein lengths, across varying hydrogen enrichment levels.

The results show that the flame response exhibited very little sensitivity to  $\mathcal{L}$ , considering the range of  $\mathcal{L}$  achievable in practical combustion systems. We note that this present study is restricted to laminar flames;  $\mathcal{L}$  variations may play a larger role in the response of turbulent flames, where flame wrinkling is substantial.

#### 4.3. General Sensitivity Analysis

Insights into the effect of hydrogen enrichment on the flame response can be obtained by performing an analysis of the sensitivity of  $\mathcal{F}$  to the properties  $s_{L0}$ ,  $\mathcal{L}$  and  $\bar{u}_1$ . The analysis was conducted at  $(\varphi, \beta) = (0.8, 0.071)$  for two cases:  $\eta_H = 0$  and  $\eta_H = 0.6$ , in order to obtain two FTFs upon which comparisons may be made. The Markstein lengths used were the actual values in literature [58].

To attempt to isolate the effects of different parameters, the  $\eta_H = 0$  case was then artificially modified in order to perform three separate simulations, where the variables  $s_{L0}$ ,  $\mathcal{L}$  and  $\bar{u}_1$  were changed in turn to match those of the  $\eta_H = 0.6$  case. The other variables were left unchanged. This was done in order to observe the extent to which the artificially modified FTFs shifted

from the  $\eta_{\text{H}} = 0$  reference case toward the  $\eta_{\text{H}} = 0.6$  reference case, and hence determine the relative importance of each variable in governing the flame response.

Table 3 summarises the simulations performed for the sensitivity analysis. Results from  $16 \times 5 = 80$  simulations were used for this.  $\bar{Q}$  was found to vary as a result of artificially modifying the base parameters, but this variation was not significant.

Table 3: Summary of simulation parameters for the sensitivity analysis.

$\varphi$	$\eta_{\text{H}}$	$\beta$	$f_{\text{p}}$ [Hz]	$\bar{u}_1$ [m s <sup>-1</sup> ]	$s_{\text{L0}}$ [*2] [m s <sup>-1</sup> ]	$\mathcal{L}$ [mm]	$\bar{Q}$ [kW]
0.8	0.0	0.071	10:10:160	2.7878	0.2742	0.56	2.69
0.8	0.6	0.071	10:10:160	2.8069	0.4922	-0.11	2.69
0.8	[*1]	0.071	10:10:160	2.8069	0.2742	0.56	2.71
0.8	[*1]	0.071	10:10:160	2.7878	0.4922	0.56	2.67
0.8	[*1]	0.071	10:10:160	2.7878	0.2742	-0.11	2.69

[\*1] Simulations with artificially modified parameters.

[\*2] Evaluated by Cantera, see Section 3.3 for details.

Figure 12 shows the results of the sensitivity analysis. It is clear that the laminar flame speed,  $s_{\text{L0}}$ , is the dominant cause of the FTF/FDF shift at elevated hydrogen enrichment, while the effects of  $\bar{u}_1$  and  $\mathcal{L}$  are minimal. Note that the  $\eta_{\text{H}} = 0$  reference curve overlaps the modified  $\bar{u}_1$  and  $\mathcal{L}$  curves to the point where the three curves are indistinguishable across the majority of the frequency range. The same is true for the  $\eta_{\text{H}} = 0$  reference and the modified  $s_{\text{L0}}$  curves.

The insensitivity of  $\mathcal{F}$  to  $\bar{u}_1$  is an expected result for these test cases, since both of these base variables do not change significantly in absolute terms across the  $\eta_{\text{H}} = 0$  and  $\eta_{\text{H}} = 0.6$  cases. While  $\bar{u}_1$  is calculated based on the fuel mixture density and heating value in order to satisfy a constant power constraint, it changes negligibly with  $\eta_{\text{H}}$  since the dominant mass component in the fuel mixture is air. This implies that  $\mathcal{F}$  may change significantly with  $\bar{u}_1$  if differences in their absolute values become significantly large, but for lean premixed gaseous fuels, this is unlikely to be the case.

The insensitivity of  $\mathcal{F}$  to  $\mathcal{L}$  is supported by the study conducted in Section 4.2, which suggested that flame wrinkling in laminar flames was not substantial enough for variations in  $\mathcal{L}$  to drive significant changes in the flame response.

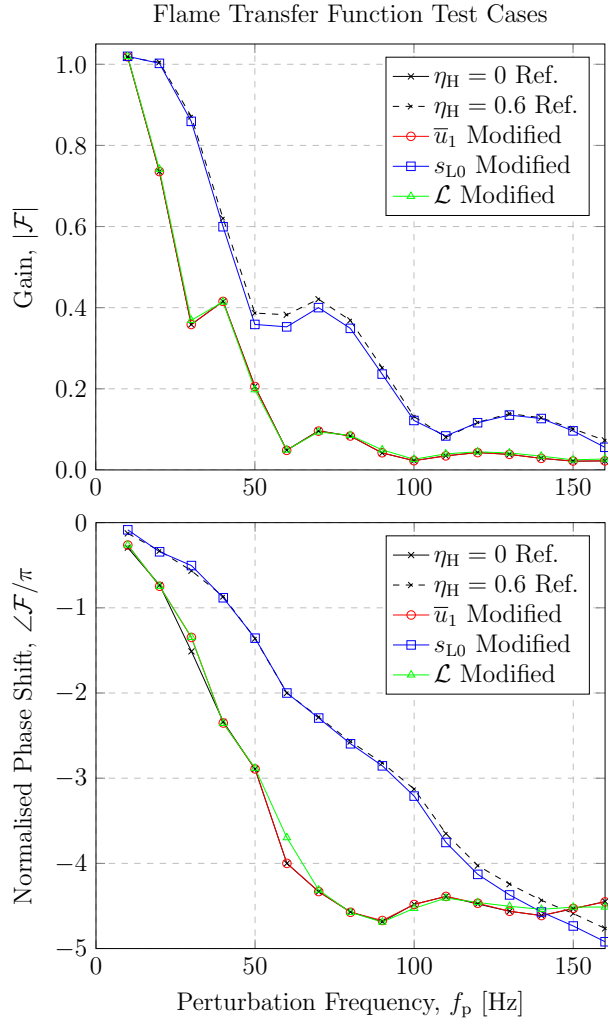


Figure 12: Flame speed is the dominant driver of hydrogen-enriched flame response.

## 5. Conclusion

The enrichment of conventional methane fuel with hydrogen causes significant changes to several of its base properties, the most significant being laminar flame speed which increases from  $0.386 \text{ m s}^{-1}$  at zero hydrogen enrichment to  $1.218 \text{ m s}^{-1}$  at 80% hydrogen enrichment (at equivalence ratio 1.08). This study has investigated the effect of hydrogen enrichment on the forced response of the flame in the context of thermoacoustic stability. Across hydrogen enrichment levels ranging from 0% to 80% and with the flame's thermal power maintained constant, it was found that with increasing hydrogen enrichment, the frequency fall off of the flame's gain was pushed to higher frequencies, as was the frequency at which nonlinear effects became important. The phase lag in the flame's response reduced with hydrogen enrichment level, in accordance with the shortening of the mean flame shape, since the convection time between the flame base and the flame front is reduced.

Further investigations showed that changes to the base laminar flame speed  $s_{L0}$  were by far the dominant factor underpinning the changes in the forced flame response. Variations in Markstein length  $\mathcal{L}$  were found to have no practical effect on the results. This is important because the Markstein lengths of mixtures containing multiple fuel components of different molecular diffusivities are difficult to predict with theory, and few studies have attempted to do this specifically for  $\text{CH}_4/\text{H}_2/\text{Air}$  blends. This work shows that a precise prediction of the Markstein length may not be critical within the scope of practical engineering application.

Analysis of the flame dynamics suggested that the higher frequency fall off of the flame's gain with hydrogen enrichment was linked to a higher resistance to distortion due to the higher flame speed. The increased resistance to flame distortion suggests that the turbulent flames may behave in a similar manner, provided the hydrogen-enrichment level is high enough.

The higher gain fall-off frequency of hydrogen-enriched flames suggests a generally higher propensity to thermoacoustic instability. In practice, changes in the phase response of the flame will also play a role, and these will depend on the geometry of the combustor within which the flame is placed; this is consistent with the observation that hydrogen enrichment can inhibit thermoacoustic oscillations in some combustors [11, 52].

## **Acknowledgements**

This work is supported by the Beit Fellowship Trustees of Imperial College London and the European Research Council (ERC) Consolidator Grant AFIRMATIVE (2018-23).

## References

- [1] WEC, Hydrogen an Enabler of the Grand Transition—Future Energy Leader Position Paper, Technical Report, 2018.
- [2] H. Council, How Hydrogen Empowers the Energy Transition, Technical Report, Brussels, Belgium, 2017.
- [3] IEA, The Future of Hydrogen: Seizing Today’s Opportunities, Technical Report, 2019.
- [4] IRENA, Hydrogen from Renewable Power: Technology Outlook for the Energy Transition, Technical Report, 2018.
- [5] J. Hord, Is hydrogen a safe fuel?, *International journal of hydrogen energy* 3 (1978) 157–176. URL: [http://dx.doi.org/10.1016/0360-3199\(78\)90016-2](http://dx.doi.org/10.1016/0360-3199(78)90016-2). doi:10.1016/0360-3199(78)90016-2.
- [6] R. D. MacCarty, J. Hord, H. M. Roder, Selected properties of hydrogen (engineering design data), volume 168., Washington, 1981.
- [7] S. Taamallah, K. Vogiatzaki, F. M. Alzahrani, E. M. A. Mokheimer, M. A. Habib, A. F. Ghoniem, Fuel flexibility, stability and emissions in premixed hydrogen-rich gas turbine combustion: Technology, fundamentals, and numerical simulations, *Applied energy* 154 (2015) 1020–1047. URL: <http://dx.doi.org/10.1016/j.apenergy.2015.04.044>. doi:10.1016/j.apenergy.2015.04.044.
- [8] P. Griebel, Gas Turbines and Hydrogen, *Hydrogen Science and Engineering : Materials, Processes, Systems and Technology*, Wiley-VCH Verlag GmbH & Co. KGaA, Weinheim, Germany, 2016, pp. 1011–1032. URL: <https://onlinelibrary.wiley.com/doi/abs/10.1002/9783527674268.ch43>. doi:10.1002/9783527674268.ch43.
- [9] İlker Yilmaz, A. Ratner, M. Ilbas, Y. Huang, Experimental investigation of thermoacoustic coupling using blended hydrogen–methane fuels in a low swirl burner, *International journal of hydrogen energy* 35 (2010) 329–336. URL: <http://dx.doi.org/10.1016/j.ijhydene.2009.10.018>. doi:10.1016/j.ijhydene.2009.10.018.

- [10] O. Choi, M. C. Lee, Investigation into the combustion instability of synthetic natural gases using high speed flame images and their proper orthogonal decomposition, *International journal of hydrogen energy* 41 (2016) 20731–20743. URL: <http://dx.doi.org/10.1016/j.ijhydene.2016.09.201>. doi:10.1016/j.ijhydene.2016.09.201.
- [11] J. Zhang, A. Ratner, Experimental study of the effects of hydrogen addition on the thermoacoustic instability in a variable-length combustor, *International journal of hydrogen energy* (2021). URL: <http://dx.doi.org/10.1016/j.ijhydene.2021.02.063>. doi:10.1016/j.ijhydene.2021.02.063.
- [12] T. Poinsot, Prediction and control of combustion instabilities in real engines, *Proceedings of the Combustion Institute* 36 (2017) 1–28. URL: <http://dx.doi.org/10.1016/j.proci.2016.05.007>. doi:10.1016/j.proci.2016.05.007.
- [13] S. Candel, Combustion dynamics and control: Progress and challenges, *Proceedings of the Combustion Institute* 29 (2002) 1–28. URL: [http://dx.doi.org/10.1016/S1540-7489\(02\)80007-4](http://dx.doi.org/10.1016/S1540-7489(02)80007-4). doi:10.1016/S1540-7489(02)80007-4.
- [14] V. Yang, T. Lieuwen, *Combustion Instabilities In Gas Turbine Engines: Operational Experience, Fundamental Mechanisms, and Modeling*, volume 210, American Institute of Aeronautics and Astronautics, Reston, VA, 2006. URL: <http://arc.aiaa.org/doi/abs/10.2514/4.866807>. doi:10.2514/4.866807.
- [15] T. C. Lieuwen, *Gas turbine emissions*, volume 38, Cambridge Univ. Press, Cambridge [u.a.], 2013. URL: [http://bvbr.bib-bvb.de:8991/F?func=service&doc\\_library=BVB01&local\\_base=BVB01&doc\\_number=026225752&sequence=000004&line\\_number=0002&func\\_code=DB\\_RECORDS&service\\_type=MEDIA](http://bvbr.bib-bvb.de:8991/F?func=service&doc_library=BVB01&local_base=BVB01&doc_number=026225752&sequence=000004&line_number=0002&func_code=DB_RECORDS&service_type=MEDIA).
- [16] D. R. Ballal, A. H. Lefebvre, *Gas turbine combustion: alternative fuels and emissions*, CRC Press, 2010. URL: <http://www.vlebooks.com/vleweb/product/openreader?id=none&isbn=9781420086058>.
- [17] P. Jansohn, *Modern Gas Turbine Systems*, volume 20, Elsevier Science & Technology, Cambridge, 2013. URL: [https://ebookcentral.proquest.com/lib/\[SITE\\_ID\]/detail.action?docID=1574936](https://ebookcentral.proquest.com/lib/[SITE_ID]/detail.action?docID=1574936).



- [18] J. W. S. Rayleigh, R. B. Lindsay, *The Theory of Sound*, 2., ed. rev. and enl. ed., Dover Publ, New York, 1945.
- [19] B.-T. Chu, On the energy transfer to small disturbances in fluid flow (part i), *Acta mechanica* 1 (1965) 215–234. doi:10.1007/BF01387235.
- [20] T. Lieuwen, Modeling Premixed Combustion-Acoustic Wave Interactions: A Review, *Journal of Propulsion and Power* 19 (2003) 765–781. URL: <http://arc.aiaa.org/doi/full/10.2514/2.6193>. doi:10.2514/2.6193.
- [21] N. Noiray, D. Durox, T. Schuller, S. Candel, A unified framework for nonlinear combustion instability analysis based on the flame describing function, *Journal of Fluid Mechanics* 615 (2008) 139–167. URL: <https://dx.doi.org/10.1017/S0022112008003613>. doi:10.1017/S0022112008003613.
- [22] A. P. Dowling, S. R. Stow, Acoustic analysis of gas turbine combustors, *Journal of Propulsion and Power* 19 (2003) 751–764. URL: <http://arc.aiaa.org/doi/full/10.2514/2.6192>. doi:10.2514/2.6192.
- [23] P. Palies, *Stabilization and Dynamic of Premixed Swirling Flames*, Elsevier Science & Technology, San Diego, 2020. URL: [https://ebookcentral.proquest.com/lib/\[SITE\\_ID\]/detail.action?docID=6247860](https://ebookcentral.proquest.com/lib/[SITE_ID]/detail.action?docID=6247860).
- [24] C. Lee, S. Cant, LES of Nonlinear Saturation in Forced Turbulent Premixed Flames, *Flow, turbulence and combustion* 99 (2017) 461–486. URL: <https://www.ncbi.nlm.nih.gov/pubmed/30069156>. doi:10.1007/s10494-017-9811-4.
- [25] S. Ruan, T. D. Dunstan, N. Swaminathan, R. Balachandran, Computation of Forced Premixed Flames Dynamics, *Combustion science and technology* 188 (2016) 1115–1135. URL: <http://www.tandfonline.com/doi/abs/10.1080/00102202.2016.1174117>. doi:10.1080/00102202.2016.1174117.
- [26] X. Han, A. S. Morgans, Simulation of the flame describing function of a turbulent premixed flame using an open-source LES solver, *Combustion and flame* 162 (2015) 1778–1792. URL: <http://>

//dx.doi.org/10.1016/j.combustflame.2014.11.039. doi:10.1016/j.combustflame.2014.11.039.

- [27] S. Hermeth, G. Staffelbach, L. Y. M. Gicquel, T. Poinsot, LES evaluation of the effects of equivalence ratio fluctuations on the dynamic flame response in a real gas turbine combustion chamber, *Proceedings of the Combustion Institute* 34 (2013) 3165–3173. URL: <http://dx.doi.org/10.1016/j.proci.2012.07.013>. doi:10.1016/j.proci.2012.07.013.
- [28] S. Wysocki, G. Di-Chiaro, F. Biagioli, Effect of fuel mixture fraction and velocity perturbations on the flame transfer function of swirl stabilized flames, *Combustion theory and modelling* 19 (2015) 714–743. URL: <http://www.tandfonline.com/doi/abs/10.1080/13647830.2015.1081410>. doi:10.1080/13647830.2015.1081410.
- [29] L. Tay-Wo-Chong, W. Polifke, Large Eddy Simulation-Based Study of the Influence of Thermal Boundary Condition and Combustor Confinement on Premix Flame Transfer Functions, *Journal of engineering for gas turbines and power* 135 (2013) 21502. URL: <http://dx.doi.org/10.1115/1.4007734>. doi:10.1115/1.4007734.
- [30] P. Wolf, G. Staffelbach, L. Y. M. Gicquel, J.-D. Müller, T. Poinsot, Acoustic and Large Eddy Simulation studies of azimuthal modes in annular combustion chambers, *Combustion and flame* 159 (2012) 3398–3413. URL: <http://dx.doi.org/10.1016/j.combustflame.2012.06.016>. doi:10.1016/j.combustflame.2012.06.016.
- [31] H. J. Krediet, C. H. Beck, W. Krebs, S. Schimek, C. O. Paschereit, J. B. W. Kok, Identification of the Flame Describing Function of a Premixed Swirl Flame from LES, *Combustion science and technology* 184 (2012) 888–900. URL: <http://www.tandfonline.com/doi/abs/10.1080/00102202.2012.663981>. doi:10.1080/00102202.2012.663981.
- [32] A. Giauque, L. Selle, L. Gicquel, T. Poinsot, H. Buechner, P. Kaufmann, W. Krebs, System identification of a large-scale swirled partially premixed combustor using LES and measurements, *Journal of turbulence* 6 (2005) N21. URL: <http://www.tandfonline.com/doi/abs/10.1080/14685240512331391985>. doi:10.1080/14685240512331391985.

- [33] Y. Xia, D. Laera, W. P. Jones, A. S. Morgans, Numerical prediction of the Flame Describing Function and thermoacoustic limit cycle for a pressurised gas turbine combustor, *Combustion science and technology* 191 (2019) 979–1002. URL: <http://www.tandfonline.com/doi/abs/10.1080/00102202.2019.1583221>. doi:10.1080/00102202.2019.1583221.
- [34] R. Balachandran, B. Ayoola, C. Kaminski, A. P. Dowling, E. Mastorakos, Experimental investigation of the nonlinear response of turbulent premixed flames to imposed inlet velocity oscillations, *Combustion and Flame* 143 (2005) 37–55. URL: <https://search.datacite.org/works/10.1016/j.combustflame.2005.04.009>. doi:10.1016/j.combustflame.2005.04.009.
- [35] A. P. Dowling, A kinematic model of a ducted flame, *Journal of Fluid Mechanics* 394 (1999) 51–72. URL: <https://dx.doi.org/10.1017/S0022112099005686>. doi:10.1017/S0022112099005686.
- [36] M. Fleifil, A. M. Annaswamy, Z. A. Ghoneim, A. F. Ghoniem, Response of a laminar premixed flame to flow oscillations: A kinematic model and thermoacoustic instability results, *Combustion and Flame* 106 (1996) 487–510. URL: [http://dx.doi.org/10.1016/0010-2180\(96\)00049-1](http://dx.doi.org/10.1016/0010-2180(96)00049-1). doi:10.1016/0010-2180(96)00049-1.
- [37] S. Ducruix, T. Schuller, D. Durox, S. Candel, Combustion Dynamics and Instabilities: Elementary Coupling and Driving Mechanisms, *Journal of Propulsion and Power* 19 (2003) 722–734. URL: <http://arc.aiaa.org/doi/full/10.2514/2.6182>. doi:10.2514/2.6182.
- [38] T. Schuller, D. Durox, S. Candel, A unified model for the prediction of laminar flame transfer functions: comparisons between conical and V-flame dynamics, *Combustion and flame* 134 (2003) 21–34. URL: [http://dx.doi.org/10.1016/S0010-2180\(03\)00042-7](http://dx.doi.org/10.1016/S0010-2180(03)00042-7). doi:10.1016/S0010-2180(03)00042-7.
- [39] J. Li, A. S. Morgans, Feedback control of combustion instabilities from within limit cycle oscillations using  $H_\infty$  loop-shaping and the  $\nu$ -gap metric, *Proceedings of the Royal Society. A, Mathematical, Physical, and Engineering Sciences* 472 (2016) 20150821. doi:10.1098/rspa.2015.0821.

- [40] D. Durox, T. Schuller, N. Noiray, S. Candel, Experimental analysis of nonlinear flame transfer functions for different flame geometries, *Proceedings of the Combustion Institute* 32 (2009) 1391–1398. URL: <http://dx.doi.org/10.1016/j.proci.2008.06.204>. doi:10.1016/j.proci.2008.06.204.
- [41] G. H. Markstein, *Nonsteady flame propagation*, Pergamon Pr, Oxford (u.a.), 1964.
- [42] X. J. Gu, M. Z. Haq, M. Lawes, R. Woolley, Laminar burning velocity and Markstein lengths of methane–air mixtures, *Combustion and Flame* 121 (2000) 41–58. URL: [https://search.datacite.org/works/10.1016/s0010-2180\(99\)00142-x](https://search.datacite.org/works/10.1016/s0010-2180(99)00142-x). doi:10.1016/s0010-2180(99)00142-x.
- [43] C. M. Luzzato, R. Assier, A. S. Morgans, X. Wu, Modelling thermoacoustic instabilities of an anchored laminar flame in a simple lean premixed combustor: including hydrodynamic effects (AIAA 2013-2003), American Institute of Aeronautics and Astronautics, Reston, Jan 1, 2013. URL: <https://search.proquest.com/docview/1428368173>.
- [44] K. Kashinath, S. Hemchandra, M. P. Juniper, Nonlinear thermoacoustics of ducted premixed flames: The influence of perturbation convection speed, *Combustion and Flame* 160 (2013) 2856–2865. URL: <https://search.datacite.org/works/10.1016/j.combustflame.2013.06.019>. doi:10.1016/j.combustflame.2013.06.019.
- [45] A. J. Aspden, M. S. Day, J. B. Bell, Turbulence-chemistry interaction in lean premixed hydrogen combustion, *Proceedings of the Combustion Institute* 35 (2015) 1321–1329. URL: <http://dx.doi.org/10.1016/j.proci.2014.08.012>. doi:10.1016/j.proci.2014.08.012.
- [46] B. T. Helenbrook, C. K. Law, The role of Landau-Darrieus instability in large scale flows, *Combustion and flame* 117 (1999) 155–169. URL: [http://dx.doi.org/10.1016/S0010-2180\(98\)00098-4](http://dx.doi.org/10.1016/S0010-2180(98)00098-4). doi:10.1016/S0010-2180(98)00098-4.
- [47] D. G. Goodwin, R. L. Speth, H. K. Moffat, B. W. Weber, *Cantera: An Object-oriented Software Toolkit for Chemical Kinetics, Thermo-*

- dynamics, and Transport Processes, <https://www.cantera.org>, 2018. doi:10.5281/zenodo.1174508, Version 2.4.0.
- [48] G. P. Smith, D. M. Golden, M. Frenklach, N. W. Moriarty, B. Eiteneer, M. Goldenberg, C. T. Bowman, R. K. Hanson, S. Song, W. C. G. Jr., V. V. Lissianski, Z. Qin, Gri-mech 3.0, 2000. URL: [http://www.me.berkeley.edu/gri\\_mech/](http://www.me.berkeley.edu/gri_mech/).
- [49] C. Dong, Q. Zhou, X. Zhang, Q. Zhao, T. Xu, S. Hui, Experimental study on the laminar flame speed of hydrogen/natural gas/air mixtures, *Frontiers of Chemical Engineering in China* 4 (2010) 417–422. doi:10.1007/s11705-010-0515-8.
- [50] S. Osher, R. Fedkiw, *Level Set Methods and Dynamic Implicit Surfaces*, volume 153, Springer New York, New York, NY, 2003. URL: <https://doi.org/10.1007/b98879>. doi:10.1007/b98879.
- [51] S. Gottlieb, C.-W. Shu, Total variation diminishing Runge-Kutta schemes, *Mathematics of Computation of the American Mathematical Society* 67 (1998) 73–85. URL: <http://www.ams.org/jourcgi/jour-getitem?pii=S0025-5718-98-00913-2>. doi:10.1090/S0025-5718-98-00913-2.
- [52] B. Ge, Y. Ji, Z. Zhang, S. Zang, Y. Tian, H. Yu, M. Chen, G. Jiao, D. Zhang, Experiment study on the combustion performance of hydrogen-enriched natural gas in a dle burner, *International journal of hydrogen energy* 44 (2019) 14023–14031. URL: <http://dx.doi.org/10.1016/j.ijhydene.2019.03.257>. doi:10.1016/j.ijhydene.2019.03.257.
- [53] D. Moëll, D. Lörstad, X.-S. Bai, Numerical Investigation of Methane/Hydrogen/Air Partially Premixed Flames in the SGT-800 Burner Fitted to a Combustion Rig, *Flow, Turbulence and Combustion* 96 (2016) 987–1003. URL: <https://lup.lub.lu.se/record/1a103ba9-e1cc-43a7-b113-e051cccc7d03>. doi:10.1007/s10494-016-9726-5.
- [54] D. Moëll, D. Lörstad, X. S. Bai, LES of hydrogen enriched methane/air combustion in the SGT-800 burner at real engine conditions, volume 4B, 2018. URL: <https://lup.lub.lu.se/record/839c097e-1943-4836-bc56-153dbee17410>.

- [55] A. Valera-Medina, S. Morris, J. Runyon, D. G. Pugh, R. Marsh, P. Beasley, T. Hughes, Ammonia, methane and hydrogen for gas turbines, *Energy Procedia* 75 (2015) 118–123. URL: <https://search.datacite.org/works/10.1016/j.egypro.2015.07.205>. doi:10.1016/j.egypro.2015.07.205.
- [56] A. Valera-Medina, R. Marsh, J. Runyon, D. Pugh, P. Beasley, T. Hughes, P. Bowen, Ammonia–methane combustion in tangential swirl burners for gas turbine power generation, *Applied Energy* 185 (2017) 1362–1371. URL: <https://search.datacite.org/works/10.1016/j.apenergy.2016.02.073>. doi:10.1016/j.apenergy.2016.02.073.
- [57] D. Kim, S. Joo, Y. Yoon, Effects of fuel line acoustics on the self-excited combustion instability mode transition with hydrogen-enriched laboratory-scale partially premixed combustor, *International journal of hydrogen energy* 45 (2020) 19956–19964. URL: <http://dx.doi.org/10.1016/j.ijhydene.2020.05.074>. doi:10.1016/j.ijhydene.2020.05.074.
- [58] N. Bouvet, F. Halter, C. Chauveau, Y. Yoon, On the effective lewis number formulations for lean hydrogen/hydrocarbon/air mixtures, *International Journal of Hydrogen Energy* 38 (2013) 5949–5960. URL: <http://dx.doi.org/10.1016/j.ijhydene.2013.02.098>. doi:10.1016/j.ijhydene.2013.02.098.